Tracing mantle source variation through xenocrystic olivine in the Taupo Volcanic Zone, New Zealand: A role for lithospheric mantle in the shift from andesitic to rhyolitic compositions

Tracing mantle source variation through xenocrystic olivine in the Taupo Volcanic Zone, New Zealand: A role for lithospheric mantle in the shift from andesitic to rhyolitic compositions.

Sally Law[1], Geoffrey D. Bromiley[1], Geoff N. Kilgour[2], J. Godfrey Fitton[1]

[1]*School of GeoSciences, Grant Institute, King's Buildings, University of Edinburgh, EH9 3FE, UK*

[2]*GNS Science, Wairakei Research Centre, Private Bag 2000, Taupo, New Zealand*

**Corresponding Author* *sally.law@ed.ac.uk*

Abstract

The central Taupo Volcanic Zone (TVZ) in New Zealand, the most productive of silicic volcanic centres, is flanked by younger andesitic stratovolcanoes to the south. Small basaltic scoria cones occur along the length of the TVZ, the most primitive of which contain abundant xenocrysts, giving insight into the mantle feeding the TVZ.

Here, we present major and minor element compositions of olivine from eleven mafic eruptions spanning the length of the central and south TVZ. Olivine compositions can be divided into three major groups, based on their texture, major and minor element composition, and zoning. Group 1 olivines are Fo_{88} in the most primitive cores, with minor element concentrations consistent with magmatic origin. Group 2 olivine compositions range from $Fo_{72–88}$ but are homogeneous within individual crystals. CaO contents are consistently lower for a given forsterite content compared to group 1 olivines and are most consistent with a plutonic crystal mush origin. Group 3 olivines have core compositions of $Fo_{93-90,}$ and NiO and CaO (0.36-0.56

wt%, <0.15wt%, respectively) concentrations consistent with a primary magma or mantle-derived origin. Compositional variation within group 3 olivine allows for further characterisation of the mantle lithologies from which the crystals were sourced. Group 3 olivines from the central TVZ are lherzolite-derived, whereas group 3 olivines from the south TVZ are harzburgite-derived. However, recent whole-rock and melt inclusion data suggests that the most fertile mantle underlies the south TVZ, and the least fertile mantle underlies the inter-caldera regions of the central TVZ where caldera-forming volcanism has ceased. This is inconsistent with interpretations drawn from the olivine data. We therefore suggest that harzburgitic xenocrysts originate from old depleted sub-continental lithospheric mantle (SCLM), which is present at depths of ~30km in the south TVZ. By contrast, rifting and crustal thinning in the central TVZ has removed the SCLM, explaining why only xenocrysts of lherzolitic origin are found. The presence of depleted SCLM may act as a boundary layer inhibiting ascent of melt from the mantle, providing an explanation for lower erupted volumes in the south TVZ. Dissolution of the orthopyroxene component in harzburgite in the presence of hydrous melt satisfies major element constraints on south TVZ basalt (high SiO_2, high MgO, low CaO/Al_2O_3). Taken together, this is the first mineralogical evidence for a tectonic and lithospheric control on the shift from andesitic to rhyolitic activity in the TVZ, implying a direct link between rifting, magma composition and volcanic productivity.

Keywords: Olivine; xenocryst; basalt; mantle; arc.

1 Introduction

Arc volcanism is responsible for some of the most explosive and hazardous eruptions on Earth (Self, 2015). Typically, volcanic arcs erupt andesite composition magma. However, some arcs evolve into systems that produce large volumes of silicic magma. The causes behind why these systems evolve to produce large volumes of silicic magma are still of intense debate. Eruptions of rhyolitic material

47 are the result of large amounts of magmatic processing, including fractional crystallisation,
48 assimilation of basement rocks, and magma mixing (Annen et al., 2006; Hildreth and Moorbath,
49 1988; Wolff et al., 2015). This obscures mantle-derived features of parental arc melts, making it
50 challenging to determine the nature of magmatic processes that ultimately feed and drive large-scale
51 silicic eruptions. Constraining spatial and temporal variations in the composition of mantle source
52 regions for parental melts is key to understanding how silicic magma systems evolve. Basalt that is
53 coeval with rhyolite may have avoided most of this crustal processing, but even the most primitive
54 basaltic magmas can still be subject to deceptively large amounts of magmatic interactions, due to
55 storage in the complex MASH (melting, assimilation, storage, homogenisation) zone (Hildreth and
56 Moorbath, 1988; Lynn et al., 2017; Waight et al., 2017; Zellmer et al., 2016). Fortunately, some
57 basalts contain mantle-derived xenocrysts, which, when combined with whole-rock incompatible
58 trace element data, can facilitate evaluation of the nature of the mantle source.
59 The Taupo Volcanic Zone (TVZ), New Zealand, is well known for its frequent and often
60 explosive silicic eruptions. It is one of the most productive silicic centres worldwide (Wilson and
61 Rowland, 2016), but we still know comparatively little about the mantle that is melting beneath the
62 TVZ. As a rifted continental arc (Wilson et al., 1995), mantle melting feeding TVZ magmatism is
63 caused by thinning and rifting of the lithosphere aided by flux melting due to slab-derived fluids
64 (Gamble et al., 1993; Rooney and Deering, 2014; Stern et al., 2006; Waight et al., 2017). The arc is
65 propagating southward, with the south TVZ characterised by predominantly andesitic volcanism
66 (Fig.1). Andesite volcanism was precursory to rhyolitic volcanism in the central TVZ, as andesite
67 lavas are found in drill holes beneath ignimbrite sheets (Browne et al., 1992; Chambefort et al., 2014;
68 Price et al., 2005). Rifting and rhyolite are concentrated in the central TVZ (Fig.1) (Rowland et al.,
69 2010; Wilson and Rowland, 2016), suggesting a tectonic control on the shift from andesitic to
70 rhyolitic volcanism.

Monogenetic basalt eruptions along the length of the arc produce small scoria cones and maars (Cole, 1973; Hiess et al., 2007; Wilson et al., 1995) (Fig. 1). These often align along normal faults parallel to the main rift axis (Hiess et al., 2007), and reflect the primitive stages of magma evolution in the TVZ (Gamble et al., 1990). Basalt compositions vary along the arc. Plagioclase-dominant high-alumina basalts (HABs) are the predominant type in the central TVZ, whilst plagioclase-poor high-magnesia basalts and basaltic andesites (HMBs and HMBAs, respectively) (Gamble et al., 1990; Graham and Hackett, 1987) are the predominant type in the south TVZ. HMBs occur but are sporadic in the central TVZ. HMBs represent the most primitive magmas in the TVZ and contain abundant magnesian olivine and clinopyroxene (Cameron et al., 2010; Gamble et al., 1990; Graham and Hackett, 1987).

A compositional continuum between cool, wet, oxidised magmas in the northern parts of the central TVZ, to hot, dry, reduced magmas in the southern part of the central TVZ has been described by Deering et al. (2008, 2010). This change in composition has been attributed to variation in flux of slab-derived fluids whereby the northern central TVZ requires greater amounts of fluid flux from the subducting slab (Rooney and Deering, 2014). More recently, these changes in basalt composition have been attributed to changes in the temporal evolution of individual caldera-forming areas of the central TVZ. Basalt from intra- (Barker et al., 2020), or syn- (Zellmer et al., 2020), caldera regions is thought to be sourced from large, hydrous melt fractions in the shallow mantle that contributed to driving caldera-forming volcanism. Examples of this are found with the Okataina Volcanic Centre (OVC) in the northern portion of the central TVZ, and correspond to the cold, wet, oxidised trends observed by Rooney and Deering (2014). Basalt from inter- (Barker et al., 2020), or post- (Zellmer et al., 2020) caldera regions is thought to be sourced from smaller, drier melt fractions deeper in the mantle that do not contribute to caldera-forming volcanism. Basalt such as this occurs in inter-caldera regions in the central portion of the central TVZ, between the currently active Taupo and

Okataina volcanic centres, and corresponds to the hot, dry, reducing trends observed by Rooney and Deering (2014).

Whilst only trends in basalt composition within the central TVZ are considered by Barker et al. (2020) and Rooney and Deering (2014), comparison with basalt from the south TVZ is made by Zellmer et al. (2020) who suggested that basalt from the south TVZ is also sourced from large, hydrous melt fractions in the shallow mantle, similar to the intra-caldera basalt of the central TVZ. As the south TVZ is in the waxing stages of magmatism, it can be considered as a pre-caldera-forming setting. Accordingly, the mantle becomes progressively more depleted through the three stages of pre-, syn-, and post-caldera volcanism (Zellmer et al., 2020). Hf isotopic evidence also requires greater slab contributions in the south TVZ (Waight et al., 2017), hinting at a transition from arc-like andesitic volcanism in the south to a rifted arc in the north, with a correspondingly smaller contribution from the slab.

Here we use the composition of xenocrystic olivine from basalts from the central and south TVZ, combined with whole-rock trace element modelling, to constrain the nature of the underlying mantle source regions. Olivine is a unique petrogenetic indicator, comprising (40-90%) of the Earth's upper mantle, and is the first mineral to crystallise from almost all primary mantle melts (Foley et al., 2013). For these reasons it has been used widely to provide insight into the composition (Lynn et al., 2017; Sobolev et al., 2005) and melting regimes (e.g. extent of melting, pressure; Matzen et al., 2017; Prelevic and Foley, 2007; Sobolev and Shimizu, 1993) of the mantle. However, magmatic processing in the crust can also have a major influence on olivine composition (Herzberg et al., 2016; Lynn et al., 2017; Gleeson and Gibson, 2019), and so careful examination of olivine textures and olivine minor element chemistry is essential before making inferences on mantle compositions and/or melting regimes. Here, we use minor element chemistry of TVZ basalt-hosted olivine xenocrysts to identify overprinting due to fractionation and magma mixing. By modelling the effects of these

crustal processes, we can use the residual olivine core compositions to infer the nature of the mantle source region for TVZ basalts.

2 Analytical Techniques

We examined seven HABs, two HMBs, one HMBA and one BA (basaltic andesite) with abundant mafic glomerocrysts from the length of the TVZ (Fig.1). All samples are scoria clasts, with the exception of Ongaroto which is a sample from a lava flow. Backscatter electron (BSE) images were taken on a Zeiss SIGMA field-emission scanning electron microscope (SEM) to identify the largest and most magnesian olivines. Approximately 50 olivine crystals were selected for subsequent analysis using a Cameca SX100 electron-probe micro-analyser (EPMA) in the Grant Institute of Earth Science, University of Edinburgh, with a total of approximately 300 point analyses. Profiles across olivine crystals were mostly concentrated on the four samples containing group two and three olivine (see sample characterisation), which were collected from, respectively, Rotomakariri, Ongaroto, Waimarino and Ohakune. This decision was based on available preliminary olivine data from Allen (2011), and detailed petrographic examination of the samples. Inclusions of Cr-spinel occur in olivines from Ongaroto, Waimarino and Ohakune, and were analysed alongside olivine compositions for use with the Al-in-olivine thermometer of Wan et al. (2008). Run conditions are listed in supplementary dataset 1. Ratios of FeO to Fe_2O_3 in spinel were calculated stoichiometrically. Temperatures from olivine-spinel pairs were calculated using the equation of Wan et al. (2008), and fO_2 in olivine-spinel pairs was calculated using the equation of Ballhaus et al. (1991).

3 Sample Characterisation

Key sample characteristics are listed in Table 1. Geochemical classification is based on whole-rock compositions and petrography (Gamble et al., 1990; Hiess et al., 2007; Kósik et al., 2016). HAB is prevalent in the central TVZ (C-TVZ), whereas HMB and HMBA are prevalent in the south TVZ (S-TVZ). Samples have variable crystal content, ranging from aphyric to highly porphyritic (>30% crystals). Groundmass is aphanitic to microcrystalline, with up to 35% vesicles. Crystallising assemblages and crystal compositions are highly variable. Olivine plus clinopyroxene crystals dominate HMB assemblages, with the addition of orthopyroxene in HMBA, whereas plagioclase is the dominant phase, with minor pyroxene and olivine in HAB (Gamble et al., 1990).

Samples contain texturally diverse olivine crystals that can be divided into three groups. Table 1 shows sample locations, classifications, and olivine groups found in each sample. Group 1 olivines are euhedral phenocrysts <500µm and are present in all basalt (HMB + HAB) samples, but absent from BA and HMBA. Group 2 are large (>500µm) subhedral olivine crystals co-grown with oscillatory zoned clinopyroxene and are present in BA and HMBA. In Ohakune (HMBA), this same texture of subhedral olivine is also co-grown with orthopyroxene. Group 3 olivines, present in Waimarino and Ongaroto (both HMB), are 250µm-1mm, subhedral to euhedral, contain highly forsteritic cores, and thin (<30µm) overgrowths of microcrystalline orthopyroxene.

4 Olivine and spinel composition

Olivines from all samples show normal zoning from core to rim (Fig. 2) but can be grouped into three categories based on compositional and textural differences. All HABs contain only phenocrystic group 1 olivine. Compositions range up to Fo_{86} in the most primitive cores, with minor element concentrations consistent with magmatic olivines (De Hoog et al., 2010). NiO is <0.2 wt.% and CaO is >0.18 wt.%. Group 1 olivines show normal zoning, down to Fo_{65}, with some outliers in

Orakeikorako and Rotokawau as low as Fo_{53} (Fig. 3). Rim compositions are in equilibrium with groundmass olivine, where present (See supplementary dataset 1 for olivine chemistry). Both HMBs also contain group 1 olivine compositions. Group 1 compositions are present as microphenocrysts and in the rim zones of larger crystals with cores of higher forsterite content.

Group 2 olivines, are present in Rotomakariri (BA), Ohakune (HMBA) and Waimarino (HMB). Group 2 olivines are weakly zoned in forsterite content and minor element concentrations. Compositions range from $Fo_{72–88}$ but are homogeneous within individual crystals. Ohakune and Waimarino contain only olivines at the upper end of this range, $Fo_{85–88}$, whereas olivines in Rotomakariri span the whole range of compositions. CaO contents are low, at <0.15 wt.% (Fig. 3). This is consistently lower for a given forsterite content compared to group 1 olivines. NiO is 0.1 - 0.15 wt.% in Waimarino and Ohakune, whereas in Rotomakariri NiO is <0.07 wt.% (Fig.3). P is below detection in all group 2 olivines from Waimarino and Ohakune and is approximately 100±50 ppm in the lower-forsterite olivines in Rotomakariri. This is very close to the detection limit (<70 ppm) (see supplement 1 for analysing conditions) and is deemed insignificant. More-forsteritic olivines in Rotomakariri also have P concentrations below detection.

Group 3 olivine compositions are defined by forsterite content $Fo_{>90}$, NiO >0.3 wt.% and CaO <0.15 wt.%. Group 3 compositions are present in Waimarino and Ongaroto. In these samples, approximately 8% of olivine macrocrysts have cores of group 3 composition. The core compositions are up to $Fo_{92.5}$ and $Fo_{90.6}$ for Waimarino and Ongaroto, respectively, primitive enough ($Fo_{>90}$) to be mantle-derived (De Hoog et al., 2010). The proportion of group 3 olivines was calculated by calibrating greyscale BSE maps of polished thin sections to measured forsterite content from EPMA data. All macrocrystic olivines in a section were then traced using *imageJ* software and thresholded to reveal the proportion of olivines with cores $Fo_{>90}$. Analysis encompassed an average ~400 olivines measured per section, with 30-40 olivines containing high-forsterite ($Fo_{>90}$) cores. NiO in the high-

187 forsterite cores is up to 0.56 wt.% (4411 ppm Ni) and 0.37 wt.% (2904 ppm Ni) in Waimarino and
188 Ongaroto, respectively (Fig.3). CaO in group 3 composition olivine cores for both samples is
189 consistently between 0.1 and 0.15 wt.% (830-1100 ppm Ca) (Fig. 3), while P is below the detection
190 limit (<70 ppm). Group 3 compositions are only present in crystal cores. The rims of olivines with
191 group 3 composition cores do not have the composition of mantle-derived olivine and are normally
192 zoned down to Fo_{64} in Ongaroto and Fo_{85} in Waimarino, correlating with decreases in NiO and
193 increases in CaO (Fig. 2). The rim composition falls into the group 1 category; however neither
194 sample contains groundmass glass or groundmass olivine, so it is not possible to assess whether rim
195 compositions were in equilibrium with the melt. Often, rims are overgrown by microcrystalline
196 orthopyroxene, suggesting disequilibrium with the final melt. Phosphorus remains below detection in
197 the rims of olivines with group 3 composition cores in Waimarino, but in Ongaroto up to 400ppm P
198 is detected in the outermost rim zones, indicative of rapid growth (Milman-Barris et al., 2008).
199 HMB samples contain olivine compositions from both groups 1 and 3. Olivines with group 3 core
200 compositions have group 1 composition rims, producing normal zoning from core to rim. HAB
201 samples only contain group 1 olivine compositions. However, there is a systematic offset in NiO
202 between group 1 compositions in HMBs and HABs, where the former show relative enrichment in
203 NiO for a given forsterite content when compared to the latter (Fig. 3). All single-crystal olivines in
204 HMB samples exhibit this trend, indicating that the process controlling the rim zonation in these
205 crystals is the same.
206 Spinel occurs as inclusions in olivine from Ongaroto (HMB), Ohakune (HMBA) and Waimarino
207 (HMB), and forms two distinct chemical trends: a Cr-Al trend and a Fe-Ti trend (Fig. 4). All three
208 samples contain spinel inclusions that fit a Cr-Al trend, whereas only Ongaroto contains additional
209 spinel that fits a Fe-Ti trend (Fig. 4d). The Cr-Al group from Waimarino and Ohakune have Mg# of
210 40−70 (atomic Mg/(Mg+Fe) *100), Cr# of 70−80 (atomic Cr/(Cr+Al) *100), and TiO_2 of <0.7 wt.%.
211 Some spinel from Ongaroto also follows a Cr-Al trend, but with Cr# of 50−65. These are restricted to

212 the high-forsterite cores of group 1 Ongaroto olivines. Seven of the 14 spinels in Ongaroto olivines
213 define the Fe-Ti trend (Fig. 4), with increasing Fe^{3+} and TiO_2, towards the rims of the host olivine.
214 Spinel from the Fe-Ti group overlap magmatic fractionation trends, with Mg# and Cr# decreasing
215 with forsterite content of the host olivine, and Fe^{3+} and TiO_2 increasing, pushing compositions
216 towards a Fe-Ti oxide.

217 4.1 Al-in-olivine thermometry

218 Spinel inclusions in Ongaroto and Waimarino olivine cores are appropriate for application of Al-in-
219 olivine thermometry (Wan et al., 2008). Ongaroto olivine-spinel pairs yield temperatures of
220 1200±40˚C (n=8, 1σ = 28˚C). Waimarino olivine-spinel pairs yield temperatures of 1168˚C ±40˚C
221 (n=8, 1σ = 24˚C). The error on the calculation (±40˚C) is larger than the error calculated in Wan et al.
222 (2008) (±20˚C) and is propagated from the error on the measurement of Al in olivine. The calculated
223 temperatures are within error of one another; however increasing the precision on the measurement
224 of Al in olivine would reduce the error on Al and could potentially reveal more information on
225 temperature shifts between samples.

226 5 Discussion

227 Magmatic processes occurring in the crust, such as fractional crystallisation, crustal assimilation and
228 magma mixing can overprint and obscure primary mantle-derived signatures in olivine (Gleeson and
229 Gibson, 2019; Herzberg et al., 2016; Lynn et al., 2017). To circumvent the effects of these processes
230 to determine mantle-derived signatures, we have modelled the effects of fractional crystallisation and
231 magma mixing on the olivine cargo in order to filter out those olivines that have been affected. The
232 remaining olivines are then assessed for their potential to be mantle-derived xenocrysts, in light of
233 alternative models for producing high-Fo, high-Ni olivines (Matzen et al., 2017, 2013; Rowe and
234 Tepley, 2016; Sobolev et al., 2005; Straub et al., 2011).

5.1 Crustal processing

To test the effect of fractional crystallisation on olivine composition we conducted forward models of crystallisation using *Petrolog* (Danyushevsky and Plechov, 2011). We simulate crystallisation of olivine in the absence of other phases as this is the only macrocryst phase in Ongaroto, and the first phase to form in all other magmas (Gamble et al., 1990). This simplifies the model by allowing $D_{bulk} = D^{Ni}_{Ol/melt}$. Partitioning of Ni into olivine is dependent on multiple factors, including temperature, and melt composition (Beattie, 1993; Matzen et al., 2013, 2017), specifically melt MgO and SiO_2. These factors are difficult to deconvolve, as MgO is often a proxy for temperature, and SiO_2 is strongly linked to melt polymerisation, which may be an underlying control on partitioning behaviour. Equations to calculate $D^{Ni}_{Ol/melt}$ in Putirka et al. (2011) account for variation in SiO_2, MgO and temperature in the melt. Using a natural, near-primary HMB composition from Gust and Perfit (1987), adapted to be in Fe-Mg equilibrium (Roeder and Emslie, 1970) with the most primitive non-mantle olivines from the TVZ (Fo_{90}), and a temperature of 1200°C from olivine spinel thermometry, gives a $D^{Ni}_{Ol/melt} = 8$. The input composition for this calculation is given in supplementary dataset 1. As Ni becomes more compatible with decreasing melt MgO, this value is a minimum, and non-primary melts with lower MgO crystallising olivine will have higher values of $D^{Ni}_{Ol/melt}$, up to ~15.

The model was run at 5 kbar as a representative depth for the mid crust in the TVZ (Stratford and Stern, 2006); running the model at 10 kbar and 1 kbar showed it to be insensitive to changes in pressure. The model was run until 30% fractional crystallisation had occurred, at which point the equilibrium olivine matched the least forsteritic compositions noted in the sample suite. Group 1 olivine compositions, which encompass all the olivine in HABs, are consistent with the results of simple fractional crystallisation modelling (Fig. 5). The maximum forsterite content measured in these olivines shows that they crystallised from a melt that had already extensively fractionated olivine. There is no record of the earlier stages of olivine fractionation in HAB samples. This is

consistent with the notion that HABs represent melts that experienced earlier fractionation and removal of more primitive olivine, and that they are not primary basalts (Gust and Perfit, 1987; Sisson and Grove, 1993).

Group 2 olivines in Rotomakariri and Ohakune are also consistent with prior fractionation of olivine, despite their low CaO contents. NiO contents are constant from core to rim, which suggests equilibration of NiO across the crystal. Therefore, group 2 olivines are derived from primitive but non-primary melts that have experienced variable degrees of fractionation and are well equilibrated to produce flat forsterite and NiO trends from core to rim.

Group 1 olivine compositions in Waimarino and Ongaroto have Fo vs. NiO trends that are offset to higher NiO at lower Fo and cannot be explained by simple crystal fractionation (Fig. 5a). This offset is observed in all group 1 olivine compositions in both Waimarino and Ongaroto samples, and therefore occurs in the mid to rim zones of olivines with group 3 composition cores (indicated by translucent (mid zones) and hollow (rims) symbols in Fig. 5), and also throughout the group 1 olivines. The core-rim compositional trend in olivines with group 3 cores and group 1 rims runs less steeply counter to the primary magma fractionation trend (Fig. 5). The lowest-forsterite zones show the greatest enrichment in NiO when compared to the modelled fractional crystallisation trend (Fig. 5a), suggestive of a magmatic control. Alternate episodes of fractionation and magma recharge can produce elevated NiO contents in olivines at lower forsterite content (Fig. 5b). Gleeson and Gibson (2019) produced a numerical model showing that NiO enrichment in fractionated olivines in ocean-island basalt can arise as a result of multiple episodes of magma recharge. Here we have adapted their model to reflect crystallisation of olivine in conditions appropriate for the TVZ.

Using the same primary magma composition and D value as above, we ran models of fractional crystallisation (for full model parameters see supplementary dataset 1) in which batches of fresh magma of the initial composition were added repeatedly when the temperature had fallen by 200˚C. Each recharge event involved the addition of a batch of magma with a volume equal to the initial

volume, meaning that for each subsequent recharge event, the ratio of fresh melt to fractionated melt would decrease, and hence the influence of the recharge event on the melt would also decrease with time. After each recharge event the composition of the mixed magma composition was used to start the next iteration of fractionation. This model effectively reproduces the enrichment in NiO observed in group 1 olivine in Ongaroto and Waimarino (Fig. 5b). It suggests that injection of multiple batches of mantle-derived magma contributed to the final composition of the erupted magma, and has overprinted the composition of the mid to rim zones of the olivines. The temperature interval of 200°C between iterations of the model is a relatively unconstrained variable. Reducing the temperature interval in which each fractionation iteration is run means less fractionation would occur between recharge events, and therefore more iterations of repeated fractionation and recharge would be required to reach a given high-NiO, low-Fo composition. While this means that the model is not able to quantify the number of recharge events required to produce a specific composition, it is useful in revealing cryptic signs of magma mixing in these highly primitive magmas. However, we acknowledge that the more recharge events that are required creates a larger space problem. In the TVZ it is well documented that the injection into the crust of large volumes of basaltic magma is required in order to drive the production of silicic magma. Despite the small erupted volume of the HMB magma, the HMB samples represent only a small fraction of the total magma volume. However, in other magmatic settings, where flux of magma from the mantle is significantly lower, this may not be a viable mechanism for explaining olivine compositions.

5.2 Mantle Origin of Olivine Cores and Cr-Spinel inclusions

Fo and NiO contents in group 3 olivine cores from Ongaroto and Waimarino ($Fo_{90–93}$; 0.33-0.56 wt.% Ni) are too high for them to have crystallised from a fractionated mantle-derived melt. Group 3 compositions have forsterite contents ($Fo_{>90}$) that reflect either crystallisation of olivine from a primitive or primary mantle melt, or residual olivine from a mantle lithology. Group 3 Olivine cores

from Ongaroto have compositions that overlap with mantle lherzolite (Fig. 5). However, their compositions could also be in equilibrium with a primary mantle melt derived from partial melting of lherzolite. Group 3 Ongaroto olivine cores contain numerous small spinel inclusions of Mg-chromite composition, with $Cr\#_{56\text{-}70}$, typical of mantle lherzolite (Arai, 1994; Ballhaus et al., 1991; Workman and Hart, 2005). However, Barker et al. (2020) report olivines in Ongaroto with compositions matching group 3, hosting primitive melt inclusions, suggesting a magmatic origin for these olivines. Like composition, crystal habit is not a definitive discriminant between magmatic and mantle-derived olivine. Subhedral xenocrystic olivine cores overgrown by magmatic olivine rims can produce euhedral crystals (Boudier, 1991). Olivine rims which have a magmatic, not mantle-derived composition, record periods of basaltic fractionation and repeated episodes of magma recharge. This could explain the euhedral shape of olivines with group 3 composition cores, if the cores were mantle-derived (Boudier, 1991). However, the presence of melt inclusions in Fo_{90} composition olivine reported by Barker et al. (2020) strongly suggests a magmatic origin of the group 3 composition cores in Ongaroto. The melt that these olivines crystallised from must have been derived from a lherzolite source rock, with minimal fractionation prior to crystallisation of the group 3 cores, in order to remain in equilibrium with the lherzolite mantle and retain such high NiO contents.

Waimarino olivine cores with Fo and NiO contents that are too high for them to be xenocrysts entrained in the melt from mantle lherzolite (Fig. 5) also contain highly refractory Cr-spinel (Cr# 70−80) (Fig. 4). It has been suggested (Sobolev et al., 2005) that olivine phenocrysts with similar compositions ($Fo_{91–93}$; NiO > 0.45 wt.%) in basalt from plume settings crystallised from magma derived from pyroxenite lithologies in the mantle, because lower bulk D_{Ni} in the olivine-free pyroxenite leads to enrichment of Ni in the partial melt. Pyroxenite xenoliths are found in a range of tectonic settings, so it is possible that the mantle beneath the TVZ is not composed solely of peridotite but contains veins of pyroxenite. It then follows that the high NiO content of the olivine

could be due to a higher NiO content in the primary magma resulting from melting an olivine-free source (Straub et al., 2008; 2011; 2014).

The solidi of pyroxenite and peridotite are similar in the presence of water, but melt productivity is higher for pyroxenite at a given temperature and pressure (Sorbadere et al., 2013), especially if these are present as veins in a much more voluminous peridotite matrix. Therefore, a relatively small proportion of pyroxenite in the source can have a large effect on the relative proportion of melt supplied by pyroxenite and peridotite and hence on the aggregate melt composition. We modelled a hypothetical melting scenario of a mixed pyroxenite-peridotite source for south TVZ samples to test whether a pyroxenite contribution to South TVZ magma would be consistent with observed trace element compositions. The pyroxenite:peridotite ratio was assumed to be 1:9. Melt fractions were assumed to be 0.6 and 0.1 for pyroxenite and peridotite, respectively. The modelled pyroxenite-peridotite mixed composition is shown as the thick black line on the primitive-mantle-normalised abundance diagrams in Figure 6. Given these assumptions, the model shows that a pyroxenite contribution can reasonably explain the whole-rock trace element composition of the south TVZ samples. Increasing the proportion of pyroxenite in the source produces overall lower concentrations of trace elements in the melt, due to the higher productivity of pyroxenite (Sorbadere et al., 2013), and also has the effect of decreasing concentrations of REE to a greater extent than LILE, due to the overall increased compatibility of REE in pyroxenite over an olivine-dominated mantle source. The maximum proportion of pyroxenite in the source that satisfies the trace element profiles of south TVZ samples is approximately 40% pyroxenite to 60% peridotite. Therefore, a wide range of pyroxenite in the source could satisfy the trace element budget of south TVZ samples. However, south TVZ samples also have high MgO content at high SiO_2, and low CaO/Al_2O_3 ratios (Gamble et al., 1993; Graham and Hackett, 1987). Experiments show that pyroxenite-derived melts have similar major element compositions to MORB but cannot produce melts that have both high SiO_2 and high MgO, with low CaO/Al_2O_3 (Lambart et al., 2009, 2013).

Alternatively, the higher nickel content in Waimarino olivine could be associated with the dependence of $D^{Ni}_{Ol/melt}$ on temperature. Matzen et al. (2013, 2017) showed that $D^{Ni}_{Ol/melt}$ decreases with increasing temperature, emphasising the importance of ΔT between the source and storage region on the compatibility of Ni. For example, a decrease of 100˚C results in a 0.05 wt.% increase in NiO in crystallising olivine. If the high-Ni olivines were magmatic, D_{Ol}^{Ni}=8 (Putirka et al., 2011) would require that the Ongaroto olivines crystallised from a magma with approximately 400 ppm Ni. Although whole-rock concentrations of Ni are ~140ppm for Ongaroto, a value of 400ppm Ni in the magma would approximate a typical primary mantle melt, in line with the highly primitive nature of the Ongaroto olivine cores. For Waimarino, a melt with 700 ppm Ni would be required to produce olivines containing 0.56 wt.% NiO. This is significantly higher than a typical primary mantle melt, and the whole-rock Ni content of 340ppm for Waimarino, and constitutes a predicted difference in the Ni content of the magma of 300 ppm between the two samples. Assuming no significant variation in primary melt MgO, which also controls $D^{Ni}_{Ol/melt}$, this variation in melt composition could be produced by a reduction in $D^{Ni}_{Ol/melt}$ from 8 to approximately 3.7. This corresponds to a temperature difference between the source of Ongaroto olivine and the source of Waimarino olivine of approximately 540˚C (Matzen et al., 2017). Such a large difference in temperature between Ongaroto and Waimarino mantle sources this large is not feasible. Additionally, Al-in-olivine thermometry (Wan et al., 2008) yields core temperatures of 1200˚C +/- 40˚C for Ongaroto and 1168˚C +/- 40˚C for Waimarino. Therefore, it seems unlikely that the variation in NiO in the Ongaroto vs. Waimarino olivine is due to temperature alone.

It is more likely that Ni-rich forsteritic cores from Waimarino olivines represent xenocrysts derived from depleted mantle. To test this, we took the composition of the depleted MORB mantle (DMM; Workman and Hart, 2005) and ran a melting model using MELTS (Asimow and Ghiorso, 1998; Ghiorso and Sack, 1995) similar to that of Hirschmann et al. (1998). Pressure in the model was set at 1 GPa, corresponding to the base of the crust beneath the TVZ (Stratford and Stern, 2006), and

383 fO_2 at QFM+1, corresponding to fO_2 values determined using the spinel oxygen barometer of
384 Ballhaus et al., (1991) (Fig. 4). Temperature was increased at 1˚C intervals until 20% melting had
385 occurred. At 15% melt, all clinopyroxene had melted (Fig. 5), resulting in a harzburgitic residue. A
386 detailed discussion of the use of MELTS to model peridotite melting can be found in Hirschmann et
387 al. (1998). The model simultaneously reproduces the observed increase in Ni and forsterite content
388 between the lherzolite-derived olivine cores from Ongaroto and the high-Fo, high-Ni cores from
389 Waimarino, suggesting that the Waimarino cores are most likely harzburgite-derived xenocrysts.
390 Decreasing the availability of Fe^{2+}, and therefore the total Fe that can be incorporated into olivine, by
391 increasing fO_2 to QFM+2 (Rowe and Tepley 2016), exaggerates this trend and produces similar
392 increases in Fo and Ni at 1 mol.% higher Fo for a given melt fraction. Therefore, high Ni cores from
393 Waimarino more likely reflect previous high volumes of melt extraction on residual mantle olivine,
394 rather than any chemical heterogeneities in the source region for TVZ basalts. This result suggests
395 that high-Ni, high-Fo cores from Waimarino olivines may be harzburgite-derived mantle xenocrysts.

396 ## 5.3 Low-Ca olivine

397 Group 2 olivines in Ohakune and Rotomakariri have forsterite and NiO contents consistent with
398 fractionation from a primary mantle melt (Fig. 5, section 5.1). However, they also have CaO
399 concentrations (<0.15 wt.%) lower than expected for magmatic olivine (Foley et al., 2013). Group 2
400 olivines are largely unzoned, suggesting sufficient time was available for Fe-Mg diffusion and re-
401 equilibration. CaO concentrations are constant over a range of forsterite contents (Fig. 2).
402 Historically, based on the work of Simkin and Smith (1970), low CaO (<0.1 wt.%) olivines have
403 been assumed to have mantle origin. In Rotomakariri, individual, compositionally homogeneous
404 grains of olivine exist within glomerocrysts, but with forsterite content varying from 82 to 73 mol.%
405 between glomerocrysts. In all of these glomerocrysts, and in Ohakune individual and glomerocrystic
406 olivines, CaO is constant and <0.15 wt.%. This consistency in Ca across a range of forsterite contents

in separate crystals suggests that the factor controlling low Ca is magmatic, and that these crystals are not overgrown mantle xenocrysts.

The Ca content of magmatic olivine is sensitive to melt composition, crystallisation of coexisting phases (Herzberg, 2011; Kamenetsky et al., 2006; Li et al., 2012), temperature (Köhler and Brey, 1990) and H_2O content (Gavrilenko et al., 2016) of the melt. Low Ca due to elevated H_2O is unlikely as this does not fit with measurements of relatively low H_2O contents from melt inclusions in the south TVZ (Kilgour et al., 2013). Textural evidence also suggests a common cause of low Ca between the Ohakune (south TVZ) and Rotomakariri (northern central TVZ) olivines. Furthermore, there is also scant evidence for significant variation in magmatic temperature between samples with low-Ca olivine, and those with higher Ca. Evidence for the origin of low-Ca olivine can be found in the glomerocrysts in which they occur. These glomerocrysts are antecrystic and consistent with being sourced from deep mafic/ultramafic cumulates. Two-pyroxene thermobarometry on Ohakune glomerocrysts indicates storage pressures of 4.8-5.4 kbar, corresponding to depths of 16-18km in the crust (Kósik et al., 2016). Clinopyroxene is the dominant co-crystallising phase; crystallisation of clinopyroxene will have strongly depleted the melts in CaO while having a lesser effect on melt MgO. Crystallisation at depth promotes clinopyroxene stability over plagioclase, consistent with plagioclase-poor, pyroxene-rich mineral assemblages observed in HMBs of the south TVZ. Therefore, group 2 Ohakune and Rotomakariri olivines with low Ca are more likely to be antecrystic, sourced from a deep-rooted cumulate or crystal mush by the host magma as it ascended through the crust.

5.4 Revisiting whole-rock trace element data

The interpretation of group 3 olivine core compositions from Waimarino as harzburgite-derived xenocrysts appears at odds with recent studies on mantle source composition in the TVZ. Recent studies have inferred a change in primary melt composition between basalt from areas of active

caldera-forming volcanism and basalt from inter-caldera regions (Barker et al., 2020). An evolutionary context between these regions is implied by describing these as syn- (intra-) and post- (inter-) caldera-forming settings. Basalt erupted in syn-caldera regions feeds active caldera systems, whereas basalt erupted in post-caldera regions is erupted through old inactive calderas and does not drive larger-scale volcanism. Syn-caldera basalt is sourced from large hydrous melt fractions in the shallow mantle, whereas post-caldera basalt is sourced from smaller, drier melt fractions deeper in the mantle (Barker et al., 2020; Zellmer et al., 2020). This implies that the waxing and waning of individual caldera systems is controlled by progressive depletion of the mantle beneath the TVZ (Zellmer et al., 2020).

Olivine xenocrysts discussed in this study are associated with post-caldera basalt in the central TVZ (Ongaroto) and pre-caldera basalt from the south TVZ (Waimarino) (Table 1). The south TVZ was not discussed by Barker et al. (2020), but Zellmer et al. (2020) suggested that the south TVZ sources the largest melt fractions from the shallowest depth in the mantle of the three TVZ segments. The south TVZ can be thought of as an immature system in the waxing stages of magmatism when compared to the mature caldera-forming systems of the central TVZ. The presence of harzburgite-derived xenocrysts from the south TVZ therefore needs to be reconciled against south TVZ trace element profiles, which suggest derivation of magma from a shallow fertile lherzolite source.

A variety of whole-rock geochemical datasets are available, with varying degrees of sample overlap, to enable comparison of olivine xenocryst and melt composition, and to relate these to mantle melting processes. The studies of Barker et al. (2020) and Rooney and Deering (2014) include samples from the central TVZ, whereas samples inclusive of the south TVZ are considered by Zellmer et al. (2020) and Lee (2010), and are included in the older datasets of Gamble et al. (1993) and Graham and Hackett (1987). We have combined these datasets for six representative samples; two from the south TVZ (pre-caldera setting), two from the north-central TVZ (syn-caldera

455 setting), and two from the central TVZ (post-caldera setting), to assess whole-rock geochemical
456 trends in comparison to mantle xenocryst data.

457 Primitive-mantle-normalised incompatible element diagrams for six samples are presented in
458 Figure 6. All samples show enrichments in LILE, depletions in HFSE, and relatively flat REE trends,
459 typical of arc volcanism. Pre-caldera and syn-caldera samples show the greatest enrichments in LILE
460 and greater depletions in HFSE in comparison to post-caldera samples. Post-caldera samples show
461 only moderate enrichments in LILE and moderate depletions in HFSE. REE patterns across all
462 samples are gently sloping. Light REEs are enriched compared to heavy REEs, whereas middle
463 REEs do not show great amounts of enrichment compared to heavy REEs. Absolute concentrations
464 of REEs vary across samples, and are lowest in pre-caldera samples, higher in syn-caldera samples,
465 and higher still in post-caldera samples.

466 Batch melting of DMM (Salters and Stracke, 2004) was modelled using both garnet-bearing
467 composition representative of a deep mantle source, and spinel-bearing composition, representative
468 of a shallow mantle source, and the partition coefficients given by these authors. These are the same
469 input parameters used in the melting models of Barker et al. (2020). The addition of slab-derived
470 components was modelled by using the amphibolite-derived fluid composition and element
471 mobilities from Tatsumi and Kogiso (1997) and a subducting sediment composition from Gamble et
472 al. (1996). An average of the two compositions was used for the slab-derived fluid composition. We
473 calculated up to 10% mixing between slab-derived fluid and DMM, and subsequent batch melting of
474 these compositions up to F = 0.3. The best fit models are shaded grey and labelled in bold for each
475 sample.

476 Syn-caldera samples require approximately 5% of slab-derived fluid to produce the observed
477 enrichments in LILE and relative depletions in HFSE. Smaller melt fractions can produce the
478 enrichments in LILE, but also produce significantly higher REE concentrations than observed. All
479 REE patterns are gently sloping and consistent with melting of a shallow-mantle source. Overall, the

480 syn-caldera data can be modelled with large melt fractions from a shallow mantle source with a 5%
481 slab derived fluid contribution. Post-caldera samples have smaller enrichments in LILE and less
482 pronounced depletion in HFSE than syn-caldera samples. These samples require a smaller slab-
483 derived fluid contribution of 1-3% to reproduce observed trace element variations. They also have
484 higher overall concentrations of REE, and possibly require smaller melt fractions than syn-caldera
485 samples, although our model results overlap considerably in this respect (Fig. 6). The HREE patterns
486 in the Ongaroto samples do not require a garnet-bearing source. However, HREE profiles in the
487 Kakuki sample are steeper, and may require a small amount of garnet in the source, although they
488 cannot be modelled with either purely spinel lherzolite or garnet lherzolite melting.
489 The results of the models for syn- and post-caldera samples are largely consistent with those of
490 both Zellmer et al. (2020) and Barker et al. (2020). Syn-caldera samples require greater slab-derived
491 fluid contributions than do post-caldera samples. A reliable test of melt fraction is provided by
492 considering ratios of moderately incompatible to highly incompatible elements, such as La/Sm or
493 Zr/Nb (Fig. 7). There is no systematic difference between syn- and post-caldera samples with respect
494 to these ratios, showing that Zr co-varies with Nb concentration in the magmas, and La with Sm,
495 suggesting fractional crystallisation, rather than variation in degree of mantle melting. Additionally,
496 there is no difference in Dy/Yb between the syn- and post-caldera samples, indicating neither
497 requires garnet in the mantle source.
498 The modelling approach taken for central TVZ samples produces results that are consistent with
499 previous models. The primitive olivines from Ongaroto are consistent with trace element models that
500 suggest derivation from a lherzolite source. However, olivines from Waimarino are most consistent
501 with derivation from a harzburgite source. To test whether the melt composition of Waimarino could
502 be derived from a partial melt of harzburgite, we modelled partial melting of harzburgite with a
503 variable slab-derived component (Fig. 8), similar to models of lherzolite melting (Fig. 6). A trace
504 element profile of harzburgite was calculated by taking the residue composition of a 20% batch melt

of DM (Salters and Stracke, 2004). Slab-derived inputs were set at 10%, due to the high proportion of fluid required to partially melt a refractory source such as harzburgite, and the composition subsequently partially melted between 5 and 20%. The model reproduces LILE concentrations well (Fig. 8), due to the large slab input. However, fluid-immobile, highly incompatible elements are depleted in this model. Harzburgite is depleted in the most incompatible elements, as these partition preferentially into the melt phase during the partial melting that created the harzburgite residue. This produces low Nb and Ta concentrations in comparison to the south TVZ data. Additionally, ratios of highly/moderately incompatible elements, such as Nd/Sm are <1 in the model, whereas south TVZ data have Nd/Sm >1. This shows that south TVZ magmas cannot be sourced from slab-fluid induced melting of harzburgitic mantle. This is consistent with the major element composition of south TVZ mafic rocks. Although they have lower CaO/Al_2O_3 than central TVZ mafic rocks and higher SiO_2 for a given MgO (Graham and Hackett, 1987), they are not boninites.

The trace element composition of south TVZ rocks is better matched by models of arc-type mantle melting, similar to those that match the trace element profiles of syn-caldera samples. Whole-rock trace element profiles fit a fertile lherzolite source with a significant slab-derived input. Both Waimarino and Ohakune samples have very low and flat REE patterns, consistent with large melt fractions. These samples are indicative of shallow melting of a fertile lherzolite source with 5-10% slab-derived fluid. Therefore, the source of the harzburgite-derived olivine xenocrysts must be different to the magma source region. Additionally, fluid-induced melting of lherzolite (Fig. 6) provides a better fit to the south TVZ data than a modelled composition based on mixing of harzburgite and lherzolite (Fig.8). A profile constructed by mixing 10-50% harzburgite with lherzolite does not produce significant shifts from a lherzolite-derived profile, but still produces Nd/Sm ratios of ~1, which is lower than south TVZ samples. If harzburgite-derived melt contributed to the south TVZ magmas, it must have been limited to a small proportion of the total melt volume.

A significant difference between pre-caldera and syn-caldera samples is that pre-caldera samples have increased concentrations of Th, which is fluid immobile, in contrast to syn-caldera samples, which contain comparatively more Ba and Rb, typically fluid mobile elements. Th/Nb indicates the degree of Th enrichment, where pre-caldera samples have the highest ratios of all TVZ basalts (Fig. 7). Thorium enrichments are most easily explained by a slab sediment contribution, as opposed to a purely fluid contribution (Fig. 7). This is consistent with Hf isotope evidence (Waight et al., 2017), which again necessitates a greater sediment contribution for south TVZ basalt.

5.5 Implications for the lithosphere and mantle melting

Basalt-hosted olivines from the TVZ provide evidence for both lherzolite and harzburgite within the mantle source region. The presence of olivine xenocrysts of harzburgitic origin implies that basalt in the south TVZ has sampled regions of mantle already depleted by melting processes. In contrast, lherzolite-derived olivine cores imply that regions of the mantle sampled by the central TVZ are relatively undepleted and have not been previously affected by large-scale melting (Fig. 9). The olivine xenocryst compositions appear to conflict with whole-rock and melt inclusion data, which suggest that the mantle became more depleted with ongoing magmatism at each volcanic centre (Zellmer et al., 2020). Accordingly, the south TVZ, a pre-caldera centre, should inherit olivine xenocrysts from fertile mantle, whereas Ongaroto, a post-caldera basalt, should inherit olivine xenocrysts from depleted mantle.

The sub-continental lithospheric mantle (SCLM) beneath New Zealand is harzburgitic in composition (Scott et al., 2014), whilst the deeper asthenospheric mantle in the mantle wedge is most likely lherzolitic in composition. Crust in the south TVZ is up to ~35 km thick, in contrast to the extensively thinned crust (15 km thickness) of the central TVZ (Stern et al., 2010; Stratford and Stern, 2006). During the initial stages of magma generation, as is currently occurring in the south TVZ, slab-derived fluids initially promote melt production in the mantle wedge. As magma ascends towards the crust, melts in the south TVZ interact with depleted, harzburgitic mantle and inherit

554 xenocrysts. Interaction of hydrous basalt magma with refractory harzburgite promotes absorption of
555 orthopyroxene into the magma, whilst stabilising residual olivine (Kelemen, 1990; Mitchell and
556 Grove, 2016), resulting in magma enriched in MgO relative to CaO and Al_2O_3, as is observed in
557 HMB and HMBA from the south TVZ. The potential for deeper storage due to the presence of
558 thicker lithosphere promotes clinopyroxene stability over plagioclase, resulting in the olivine +
559 clinopyroxene +/- orthopyroxene assemblages observed in HMBs in the south TVZ (Cameron et al.,
560 2010; Graham and Hackett, 1987).

561 In contrast, as rifting progresses, as is the case in the central TVZ, the lithosphere is thinned,
562 promoting upwelling of asthenospheric mantle (Fig. 9). As such, a spatial and temporal shift occurs
563 from a subduction-flux-dominated mantle melting regime in the initial stages of magmatism, as in
564 the south TVZ, to one that is controlled by both subduction-flux and decompression melting in the
565 mature central TVZ. With ongoing rifting, the SCLM is thinned and replaced by asthenospheric
566 lherzolite, and central TVZ melts inherit olivine with this lherzolitic heritage. Lherzolite melting
567 leads to relatively enriched magma with higher concentrations of CaO and Al_2O_3, producing magma
568 similar in composition to TVZ HABs, which are concentrated in the central TVZ. Shallow storage of
569 magma resulting from thinning of the crust promotes plagioclase over clinopyroxene stability,
570 producing plagioclase-dominated mineral assemblages, similar to HABs (Gamble et al., 1990).
571 Similar models have been proposed for other continental rifts, such as the Rio Grande rift. Without a
572 slab fluid inducing melting in the mantle wedge, initial magma compositions reflect melting of
573 SCLM. With progressive rifting, compositions are derived from melting of asthenospheric mantle
574 (Fitton et al., 1991; McMillan et al., 2000), with the shift in magma composition associated with the
575 pulling apart of the continental lithosphere. In the TVZ, harzburgite-derived olivine xenocrysts from
576 the south TVZ most likely represent the interaction of basaltic melt with the depleted SCLM, rather
577 than the magma itself arising from a depleted mantle source. Large melt fractions increase the
578 reaction of refractory harzburgite (Mitchell and Grove, 2016), whilst the presence of thick SCLM

may also promote deeper storage of magma in addition to inhibiting large melt fractions reaching the surface, consistent with lower erupted volumes in the south TVZ (Wilson et al., 1995). In the central TVZ, mantle melts may become more depleted with ongoing melt extraction (Zellmer et al., 2020) whilst retaining a lherzolitic source. Basalt from both intra- and inter-caldera settings are expected to have xenocrysts of lherzolitic heritage if they were to inherit any. Additionally, it is possible that the complexity of the magma plumbing system at intra-caldera settings (Cole et al., 2014) inhibits basalt magma from retaining mantle-derived xenocrysts, whereas in inter-caldera settings where basalt magma has less interaction with the crust (Gamble et al., 1993), it is more likely to retain its primitive composition and mantle-derived xenocrysts.

6 Conclusions

Basalt-hosted xenocrysts provide a useful insight into the mantle source region of one of the most productive magmatic regions on Earth. Variation in olivine composition allows for assessment of mantle source contributions in greater detail than traditional whole-rock methods. Therefore, study of olivines within mafic rocks in other magmatic settings where changes in eruptive style are attributed to changes in mantle source may be a useful tool in assessing source composition. Magmas in the south TVZ interacted with depleted harzburgitic mantle. Whole-rock data suggest that magmas here are sourced from large melt fractions in the shallow mantle, and potentially require a greater slab sediment contribution than elsewhere in the rifted arc. Central TVZ magmas show no evidence for interaction with depleted harzburgitic mantle. Variation in the extent of slab-derived fluid input during melting is required to account for geochemical differences between syn-caldera and post-caldera basalt, with syn-caldera basalt requiring greater input from the slab. All basalt compositions from the TVZ are consistent with a spinel lherzolite mantle source with variable slab contribution. We suggest that thinning of the lithosphere in the central TVZ promotes the transition from continental arc style volcanism to rhyolitic volcanism. This implies a direct link between rifting,

603 magma composition and volcanic productivity. Although subduction promotes mantle melting due to
604 fluid flux, it is the extent of rifting that determines the mantle lithology with which the magmas
605 interact, and this rifting exerts a control on primitive magma composition and fractionation pathways
606 in the crust.

607

608 # 7 Acknowledgements

609 This work was supported by a Natural Environment Research Council E^3 DTP studentship
610 NE/L002558/1. We thank Ery Hughes and Kate Saunders for providing rock samples, Nicola Cayzer
611 for assistance with SEM and Chris Hayward with electron microprobe analysis.

References

Allen, A. (2011). Textural analysis of basalts in the Taupo Volcanic Zone, New Zealand (Unpublished Master's Thesis). University of Bristol, UK.

Annen, C., Blundy, J. D., and Sparks, R. S. J. (2006). The Genesis of Intermediate and Silicic Magmas in Deep Crustal Hot Zones. *Journal of Petrology*, 47(3):505–539.

Arai, S. (1994). Characterization of spinel peridotites by olivine-spinel compositional relationships: Review and interpretation. *Chemical Geology*, 113(3-4):191–204.

Asimow, P. D. and Ghiorso, M. S. (1998). Algorithmic modifications extending MELTS to calculate subsolidus phase relations. *American Mineralogist*, 83(9-10):1127–1132.

Ballhaus, C., Berry, R. f., and Green, D. H. (1991). High pressure experimental calibration of the olivine-orthopyroxene-spinel oxygen geobarometer: implications for the oxidation state of the upper mantle. *Contributions to Mineralogy and Petrology*, 107(1):27–40.

Barker, Rowe, M. C., Wilson, C. J. N., Gamble, J. A., Rooyakkers, S. M., Wysoczanski, R. J., Illsley-Kemp, F., and Kenworthy, C. C. (2020). What lies beneath? Reconstructing the primitive magmas fueling voluminous silici volcanism using olivine-hosted melt inclusions. *Geology*, 48(5):1–5.

Barnes, S. J. and Roeder, P. L. (2001). The Range of Spinel Compositions in Terrestrial Mafic and Ultramafic Rocks. *Journal of Petrology*, 42(12):2279–2302.

Beattie, P. (1993). Olivine-melt and orthopyroxene-melt equilibria. *Contributions to Mineralogy and Petrology*, 115(1):103–111.

Boudier, F. (1991). Olivine xenocrysts in picritic magmas. *Contributions to Mineralogy and Petrology*, 109(1):114–123.

634 Browne, P., Graham, I., Parker, R., and Wood, C. (1992). Subsurface andesite lavas and plutonic
635 rocks in the Rotokawa and Ngatamariki geothermal systems, Taupo Volcanic Zone, New Zealand.
636 *Journal of Volcanology and Geothermal Research*, 51(3):199–215.

637 Cameron, E., Gamble, J., Price, R., Smith, I., McIntosh, W., and Gardner, M. (2010). The petrology,
638 geochronology and geochemistry of Hauhungatahi volcano, S.W. Taupo Volcanic Zone. *Journal*
639 *of Volcanology and Geothermal Research*, 190(1-2):179–191.

640 Chambefort, I., Lewis, B., Wilson, C. J., Rae, A. J., Coutts, C., Bignall, G., and Ireland, T. R. (2014).
641 Stratigraphy and structure of the Ngatamariki geothermal system from new zircon U-Pb
642 geochronology: Implications for Taupo Volcanic Zone evolution. *Journal of Volcanology and*
643 *Geothermal Research*, 274:51–70.

644 Cole, J.W. (1973). High-alumina basalts of the Taupo Volcanic Zone, New Zealand. *Lithos*, 6(1):53-
645 64.

646 Cole, J.W., Deering, C.D., Burt, R.M., Sewell, S., Shane, P.A.R., Matthews, N.E. (2014). Okataina
647 Volcanic Centre, Taupo Volcanic Zone, New Zealand: A review of volcanism and synchronous
648 pluton development in an active, dominantly silicic caldera system. *Earth Science Reviews*, 128:1-
649 17.

650 Danyushevsky, L. V. and Plechov, P. (2011). Petrolog3: Integrated software for modeling
651 crystallization processes. *Geochemistry, Geophysics, Geosystems*, 12(7).

652 De Hoog, J. C. M., Gall, L., and Cornell, D. H. (2010). Trace-element geochemistry of mantle
653 olivine and application to mantle petrogenesis and geothermobarometry. *Chemical Geology*,
654 270(1-4):196–215.

655 Deering, C. D., Cole, J. W., and Vogel, T. A. (2008). A Rhyolite Compositional Continuum
656 Governed by Lower Crustal Source Conditions in the Taupo Volcanic Zone, New Zealand.
657 *Journal of Petrology*, 49(12):2245–2276.

658 Deering, C. D., Gravley, D. M., Vogel, T. A., Cole, J. W., and Leonard, G. S. (2010). Origins of
659 cold-wet-oxidizing to hot-dry-reducing rhyolite magma cycles and distribution in the Taupo
660 Volcanic Zone, New Zealand. *Contributions to Mineralogy and Petrology*, 160(4):609–629.

661 Fitton, J.G., James, D., and Leeman, W.P., (1991). Basic magmatism associated with late Cenozoic
662 extension in the western United States: compositional variations in space and time. *Journal of*
663 *Geophysical Research*, 96(B8): 13693-13711.

664 Foley, S., Prelevic, D., Rehfeldt, T., and Jacob, D. (2013). Minor and trace elements in olivines as
665 probes into early igneous and mantle melting processes. *Earth and Planetary Science Letters*,
666 363:181–191.

667 Gamble, J., Woodhead, J., Wright, I., and Smith, I. (1996). Basalt and sediment geochemistry and
668 magma petrogenesis in a transect from oceanic island arc to rifted continental margin arc: The
669 Kermadec-Hikurangi Margin, SW Pacific. *Journal of Petrology*, 37(6):1523–1546.

670 Gamble, J. A., Smith, I. E., McCulloch, M. T., Graham, I. J., and Kokelaar, B. P. (1993). The
671 geochemistry and petrogenesis of basalts from the Taupo Volcanic Zone and Kermadec Island
672 Arc, S.W. Pacific. *Journal of Volcanology and Geothermal Research*, 54(3-4):265–290.

673 Gamble, J. A., Smith, I. E. M., Graham, I. J., Peter Kokelaar, B., Cole, J. W., Houghton, B. F., and
674 Wilson, C. J. N. (1990). The petrology, phase relations and tectonic setting of basalts from the
675 taupo volcanic zone, New Zealand and the Kermadec Island arc - havre trough, SW Pacific.
676 *Journal of Volcanology and Geothermal Research*, 43(1-4):253–270.

677 Gavrilenko, M., Herzberg, C., Vidito, C., Carr, M. J., Ozerov, A., and Tenner, T. (2016). A Calcium-
678 in-Olivine Geohygrometer and its Application to Subduction Zone Magmatism. *Journal of*
679 *Petrology*, 57(9):1811–1832.

680 Ghiorso, M. S. and Sack, R. O. (1995). Chemical mass transfer in magmatic processes IV. A revised
681 and internally consistent thermodynamic model for the interpolation and extrapolation of liquid-
682 solid equilibria in magmatic systems at elevated temperatures and pressures. *Contributions to*
683 *Mineralogy and Petrology*, 119(2-3):197–212.

684 Gleeson, M. L. and Gibson, S. A. (2019). Crustal controls on apparent mantle pyroxenite signals in
685 ocean-island basalts. *Geology*, 47(4):321–324.

686 Graham, I. J. and Hackett, W. R. (1987). Petrology of Calc-alkaline Lavas from Ruapehu Volcano
687 and Related Vents, Taupo Volcanic Zone, New Zealand. *Journal of Petrology*, 28(3):531–567.

688 Gust, D. A. and Perfit, M. R. (1987). Phase relations of a high-Mg basalt from the Aleutian Island
689 Arc: Implications for primary island arc basalts and high-Al basalts. *Contributions to Mineralogy*
690 *and Petrology*, 97(1):7–18.

691 Herzberg, C. (2011). Identification of source lithology in the Hawaiian and Canary Islands:
692 Implications for origins. *Journal of Petrology*, 52(1):113–146.

693 Herzberg, C., Vidito, C., and Starkey, N. A. (2016). Nickel-cobalt contents of olivine record origins
694 of mantle peridotite and related rocks. *American Mineralogist*, 101(9):1952–1966.

695 Hiess, J., Cole, J. W., and Spinks, K. D. (2007). Influence of the crust and crustal structure on the
696 location and composition of high-alumina basalts of the Taupo Volcanic Zone, New Zealand. *New*
697 *Zealand Journal of Geology and Geophysics*, 50(4):327–342.

698 Hildreth, W. and Moorbath, S. (1988). Crustal contributions to arc magmatism in the Andes of
699 Central Chile. *Contributions to Mineralogy and Petrology*, 98(4):455–489.

Hirschmann, M. M., Ghiorso, M. S., Wasylenki, L. E., Asimow, P. D., and Stolper, E. M. (1998). Calculation of Peridotite Partial Melting from Thermodynamic Models of Minerals and Melts. I. Review of Methods and Comparison with Experiments. *Journal of Petrology*, 39(6):1091–1115.

Kamenetsky, V. S., Elburg, M., Arculus, R., and Thomas, R. (2006). Magmatic origin of lowCa olivine in subduction-related magmas: Co-existence of contrasting magmas. *Chemical Geology*, 233(3-4):346–357.

Kelemen, P. B. (1990). Reaction between ultramafic rock and fractionating basaltic magma I. phase relations, the origin of calc-alkaline magma series, and the formation of discordant dunite. *Journal of Petrology*, 31(1):51–98.

Kilgour, G., Blundy, J., Cashman, K., and Mader, H. M. (2013). Small volume andesite magmas and melt–mush interactions at Ruapehu, New Zealand: evidence from melt inclusions. *Contributions to Mineralogy and Petrology*, 166(2):371–392.

Kogiso, T., Tatsumi, Y., and Nakano, S. (1997). Trace element transport during dehydration processes in the subducted oceanic crust: 1. Experiments and implications for the origin of ocean island basalts. *Earth and Planetary Science Letters*, 148(1-2):193–205.

Köhler, T. P. and Brey, G. P. (1990). Calcium exchange between olivine and clinopyroxene calibrated as a geothermobarometer for natural peridotites from 2 to 60 kb with applications. *Geochimica et Cosmochimica Acta*, 54(9):2375–2388.

Kósik, S., Németh, K., Kereszturi, G., Procter, J., Zellmer, G., and Geshi, N. (2016). Phreatomagmatic and water-influenced Strombolian eruptions of a small-volume parasitic cone complex on the southern ringplain of Mt. Ruapehu, New Zealand: Facies architecture and eruption mechanisms of the Ohakune Volcanic Complex controlled by an unstable fissure eruption. *Journal of Volcanology and Geothermal Research*, 327:99–115.

723 Lambart, S., Laporte, D., and Schiano, P. (2009). An experimental study of pyroxenite partial melts
724 at 1 and 1.5 GPa: Implications for the major-element composition of Mid-Ocean Ridge Basalts.
725 *Earth and Planetary Science Letters*, 288(1-2):335–347.

726 Lambart, S., Laporte, D., and Schiano, P. (2013). Markers of the pyroxenite contribution in the
727 major-element compositions of oceanic basalts: Review of the experimental constraints. *Lithos*,
728 160-161(1):14–36.

729 Lee, T. R. (2010). *The thermal evolution of subduction zone lithosphere: Evidence from the chemical*
730 *development of Mt. Ruapehu and surrounding vents, New Zealand.* PhD thesis, Durham
731 University.

732 Li, C., Thakurta, J., and Ripley, E. M. (2012). Low-Ca contents and kink-banded textures are not
733 unique to mantle olivine: evidence from the Duke Island Complex, Alaska. *Mineralogy and*
734 *Petrology*, 104:147–153.

735 Lynn, K. J., Shea, T., and Garcia, M. O. (2017). Nickel variability in Hawaiian olivine: Evaluating
736 the relative contributions from mantle and crustal processes. *American Mineralogist*, 102(3):507–
737 518.

738 Matzen, A. K., Baker, M. B., Beckett, J. R., and Stolper, E. M. (2013). The temperature and pressure
739 dependence of nickel partitioning between olivine and silicate melt. *Journal of Petrology*,
740 54(12):2521–2545.

741 Matzen, A.K., Baker, M.B., Beckett, J.R., Wood, B.J., and Stolper, E.M. (2017). The effect of liquid
742 composition on the partitioning of Ni between olivine and silicate melt. *Contributions to*
743 *Mineralogy and Petrology*, 172(1):1–18.

744 McMillan, N., Dickin, A., Haag, D., (2000). Evolution of magma source regions in the Rio Grande
745 rift, Southern New Mexico. *Bulletin of the Geological Society of America*, 112(10):1582-1593.

746 Milman-Barris, M.S., Beckett, J.R., Baker, M.B., Hofmann, A.E., Morgan, Z., Crowley, M.R.,
747 Vielzeuf, D., and Stolper, E. (2008). Zoning of phosphorus in igneous olivine. *Contributions to*
748 *Mineralogy and Petrology*, 155(6):739–765.

749 Mitchell, A. L. and Grove, T. L. (2016). Experiments on melt–rock reaction in the shallow mantle
750 wedge. *Contributions to Mineralogy and Petrology*, 171(12):1–21.

751 Prelevic, D. and Foley, S. F. (2007). Accretion of arc-oceanic lithospheric mantle in the
752 Mediterranean: Evidence from extremely high-Mg olivines and Cr-rich spinel inclusions in
753 lamproites. *Earth and Planetary Science Letters*, 256:120–135.

754 Price, R. C., Gamble, J. A., Smith, I. E., Stewart, R. B., Eggins, S., and Wright, I. C. (2005). An
755 integrated model for the temporal evolution of andesites and rhyolites and crustal development in
756 New Zealand's North Island. *Journal of Volcanology and Geothermal Research*, 140(13):1–24.

757 Putirka, K., Ryerson, F. J., Perfit, M., and Ridley, W. I. (2011). Mineralogy and composition of the
758 oceanic mantle. *Journal of Petrology*, 52(2):279–313.

759 Roeder, P. L. and Emslie, R. F. (1970). Olivine-liquid equilibrium. *Contributions to Mineralogy and*
760 *Petrology*, 29(4):275–289.

761 Rooney, T. O. and Deering, C. D. (2014). Conditions of melt generation beneath the Taupo Volcanic
762 Zone: The influence of heterogeneous mantle inputs on large-volume silicic systems. *Geology*,
763 42(1):3–6.

764 Rowe, M. C. and Tepley, F. J. (2016). Origin and petrogenetic implications of anomalous olivine
765 from a Cascade forearc basalt. *American Mineralogist*, 101(8):1807-1819.

766 Rowland, J. V., Wilson, C. J., and Gravley, D. M. (2010). Spatial and temporal variations in magma-
767 assisted rifting, Taupo Volcanic Zone, New Zealand. *Journal of Volcanology and Geothermal*
768 *Research*, 190(1-2):89–108.

769 Salters, V. J. and Stracke, A. (2004). Composition of the depleted mantle. *Geochemistry, Geophysics,*
770 *Geosystems*, 5(5).

771 Scott, J. M., Waight, T. E., van der Meer, Q. H. A., Palin, J. M., Cooper, A. F., and Münker, C.
772 (2014). Metasomatized ancient lithospheric mantle beneath the young Zealandia microcontinent
773 and its role in HIMU-like intraplate magmatism. *Geochemistry, Geophysics, Geosystems*,
774 15(9):3477–3501.

775 Self, S. (2015). Explosive Super-Eruptions and Potential Global Impacts. In *Volcanic Hazards, Risks*
776 *and Disasters*, number M, pages 399–418. Elsevier.

777 Simkin, T. and Smith, J. V. (1970). Minor-Element Distribution in Olivine. *The Journal of Geology*,
778 78(3):304–325.

779 Sisson, T. W. and Grove, T. L. (1993). Temperatures and H2O contents of low-MgO high-alumina
780 basalts. *Contributions to Mineralogy and Petrology*, 113(2):167–184.

781 Sobolev, A. V., Hofmann, A. W., Sobolev, S. V., and Nikogosian, I. K. (2005). An olivine-free
782 mantle source of Hawaiian shield basalts. *Nature*, 434(7033):590–597.

783 Sobolev, A. V. and Shimizu, N. (1993). Ultra-depleted primary melt included in an olivine from the
784 Mid-Atlantic Ridge. *Nature*, 363(6425):151–154.

785 Sorbadere, F., Médard, E., Laporte, D., and Schiano, P. (2013). Experimental melting of hydrous
786 peridotite-pyroxenite mixed sources: Constraints on the genesis of silica-undersaturated magmas
787 beneath volcanic arcs. *Earth and Planetary Science Letters*, 384:42–56.

788 Stern, T. A., Stratford, W. R., and Salmon, M. L. (2006). Subduction evolution and mantle dynamics
789 at a continental margin: Central North Island, New Zealand. *Reviews of Geophysics*,
790 44(4):RG4002.

791 Stern, T. A., Stratford, W. R., Seward, A., Henderson, M., Savage, M., Smith, E., Benson, A., Greve,
792 S. and Salmon, M. L. (2010). Crust-mantle structure of the central North Island, New Zealand,
793 based on seismological observations. Journal of Volcanology and Geothermal Research, 190(1-
794 2):58-74).

795 Stratford, W. R. and Stern, T. A. (2006). Crust and upper mantle structure of a continental back-arc:
796 central North Island, New Zealand. *Geophysical Journal International*, 166(1):469– 484.

797 Straub, S. M., Gomez-Tuena, A., Stuart, F. M., Zellmer, G. F., Espinasa-Perena, R., Cai, Y., and
798 Iizuka, Y. (2011). Formation of hybrid arc andesites beneath thick continental crust. *Earth and*
799 *Planetary Science Letters*, 303(3-4):337–347.

800 Straub, S. M., LaGatta, A. B., Martin-Del Pozzo A. L., Langmuir, C. M (2008). Evidence from high-
801 Ni olivines for a hybridized peridotite/pyroxenite source for orogenic andesites from the central
802 Mexican Volcanic Belt. *Geochemistry, Geophysics, Geosystems*, 9(3):1-33.

803 Straub, S. M., Zellmer, G.F., Gomez-Tuena, A., Espinasa-Perena, R., Martin-del Pozzo, A.L., Stuart,
804 F.M., Langmuir, C.M (2014). A genetic link between silicic slab components and calc-alkaline arc
805 volcanism in central Mexico. *Geological Society Special Publication*, 385(1):31-64.

806 Sun, S.-S., McDonough, W.F. (1989). Chemical and isotopic systematics of oceanic basalts:
807 implications for mantle composition and processes. *Geological Society Special Publication,*
808 42(1):313-345.

809 Tatsumi, Y. and Kogiso, T. (1997). Trace element transport during dehydration processes in the
810 subducted oceanic crust: 2. Origin of chemical and physical characteristics in arc magmatism.
811 *Earth and Planetary Science Letters*, 148(1-2):207–221.

812 Waight, T. E., Troll, V. R., Gamble, J. A., Price, R. C., and Chadwick, J. P. (2017). Hf isotope
813 evidence for variable slab input and crustal addition in basalts and andesites of the Taupo Volcanic
814 Zone, New Zealand. *Lithos*, 284-285:222–236.

815 Wan, Z., Coogan, L.A., and Canil, D. (2008). Experimental calibration of aluminium partitioning
816 between olivine and spinel as a geothermometer. *American Mineralogist*, 93(July):1142– 1147.

817 Wilson, C. J. and Rowland, J. V. (2016). The volcanic, magmatic and tectonic setting of the Taupo
818 Volcanic Zone, New Zealand, reviewed from a geothermal perspective. *Geothermics*, 59:168–187.

819 Wilson, C. J. N., Houghton, B. F., McWilliams, M. O., Lanphere, M. A., Weaver, S. D., and Briggs,
820 R. M. (1995). Volcanic and structural evolution of Taupo Volcanic Zone, New Zealand: a review.
821 *Journal of Volcanology and Geothermal Research*, 68(1-3):1–28.

822 Wolff, J. A., Ellis, B. S., Ramos, F. C., Starkel, W. A., Boroughs, S., Olin, P. H., and Bachmann, O.
823 (2015). Remelting of cumulates as a process for producing chemical zoning in silicic tuffs: A
824 comparison of cool, wet and hot, dry rhyolitic magma systems. *Lithos*, 236-237:275–286.

825 Workman, R. K. and Hart, S. R. (2005). Major and trace element composition of the depleted MORB
826 mantle (DMM). *Earth and Planetary Science Letters*, 231(1-2):53–72.

827 Zellmer, G. F., Kimura, J.-I., Stirling, C. H., Lube, G., Shane, P. A., and Iizuka, Y. (2020). Genesis
828 of recent mafic magmatism in the Taupo Volcanic Zone, New Zealand: insights into the birth and
829 death of very large volume rhyolitic systems? *Journal of Petrology*.

830 Zellmer, G. F., Pistone, M., Iizuka, Y., Andrews, B. J., Gomez-Tuena, A., Straub, S. M., and Cottrell,
831 E. (2016). Petrogenesis of antecryst-bearing arc basalts from the Trans-Mexican Volcanic Belt:

Insights into along-Arc variations in magma-mush ponding depths, H2O contents, and surface heat flux. *American Mineralogist*, 101(11):2405–2422.

835 Table 1: Summary of key characteristics of the samples used in this study

Location	Segment	Name	Class*	Crystal content	Crystal ass.	Group.	Max. NiO
CTVZ-N	Syn	Rotokawau	HAB	25%	Pl>Cpx>Ol	1	0.14
CTVZ-N	Syn	Tarawera	HAB	<5%	Pl>Cpx>Ol	1	<0.1
CTVZ-N	Syn	Rotomakariri	BA	20%	Pl>Cpx>Ol	2	<0.1
CTVZ-N	Syn	Terrace Rd	HAB	25%	Pl>Cpx>Ol	1	<0.1
CTVZ	Post	Johnson Rd	HAB	10%	Pl>Ol>Cpx	1	<0.1
CTVZ	Post	Ongaroto	HMB	25%	Ol»Cpx=Pl	1 & 3	0.37
CTVZ	Post	Kakuki	HAB	10%	Pl>Ol»Cpx	1	0.14
CTVZ	Post	Orakeikorako	HAB	25%	Pl>Cpx=Ol	1	<0.1
STVZ	Pre	Waimarino	HMB	25%	Ol>Cpx»Pl	1, 2, 3	0.56
STVZ	Pre	Ohakune	HMBA	15%	Cpx=Opx>Ol	2	0.23

836 * HAB, high-alumina basalt; HMB, high-magnesia basalt; HMBA, high-magnesia basaltic andesite

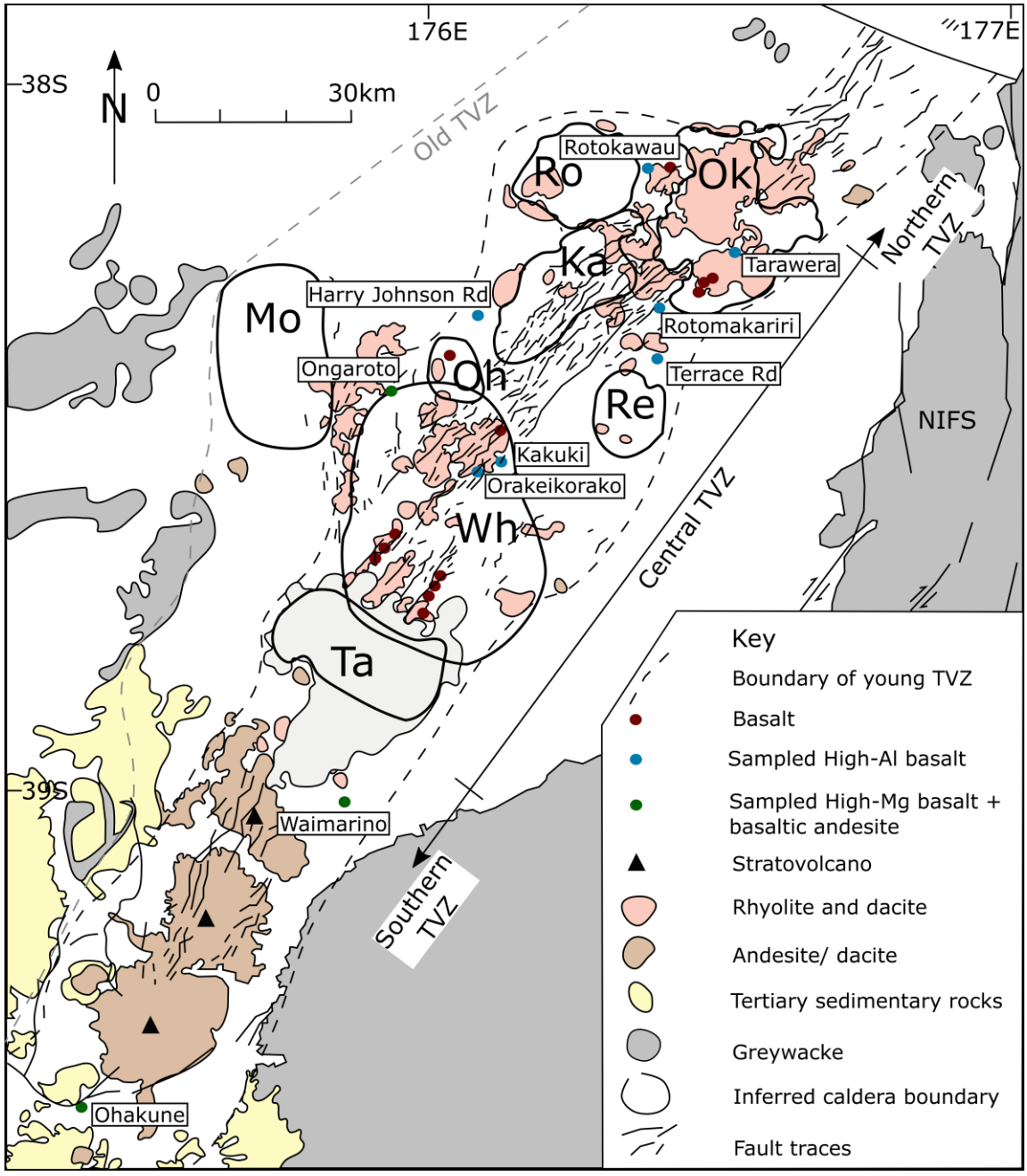

837

838 Figure 1: Map of the TVZ, modified from Wilson and Rowland (2016) and references therein. Ka -

839 Kapenga, Mo - Mangakino, Oh - Ohakuri, Ok - Okataina, Re - Reporoa, Ta - Taupo, Wh -

840 Whakamaru. NIFS - North Island Fault System. Sample coordinates are provided in supp. dataset 1.

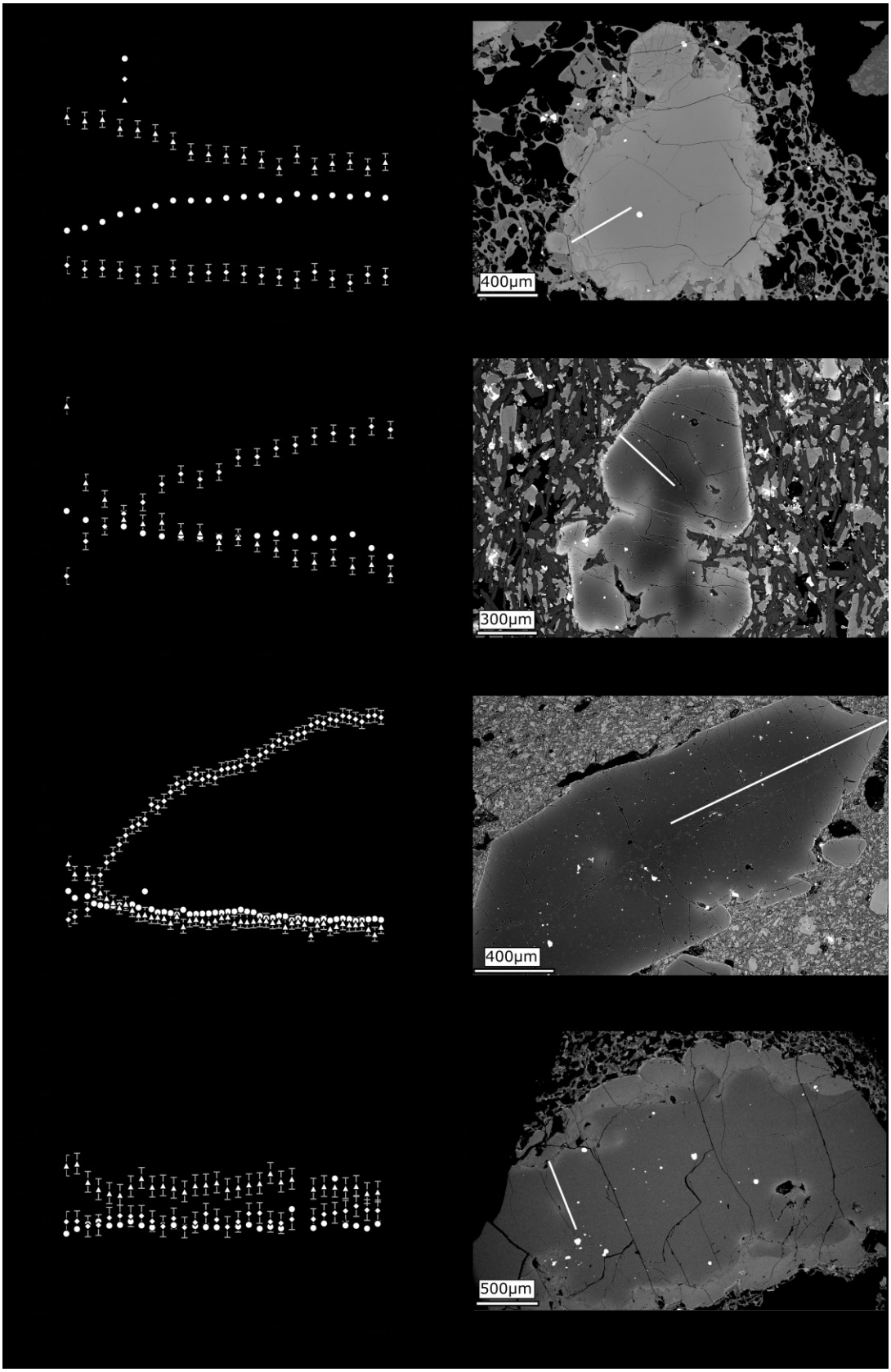

841

842 Figure 2: Examples of BSE images and compositional profiles of TVZ olivines. Rotomakariri –

843 group 2 low-Ca olivine with orthopyroxene overgrowth; Ongaroto – Group 3 high-Fo olivine core,

844 with normal zoning to group 1 phenocrystic rim; Waimarino – Group 3 high-Fo olivine core, with
845 normal zoning to group 1 phenocrystic rim; Ohakune – Group 2 low-Ca olivine with thick
846 orthopyroxene overgrowth. Note the significantly higher NiO content of group 3 Waimarino cores
847 compared with group 3 Ongaroto cores. White lines indicate location of tracks. Error bars are smaller
848 than symbols, except where shown.

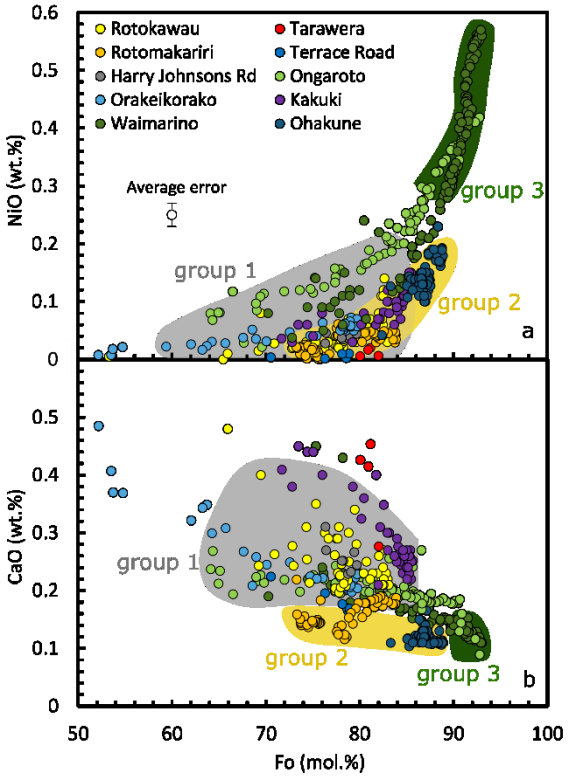

849

850 Figure 3: a) Fo vs. NiO in olivine. Note the higher concentrations of NiO at lower Fo in Ongaroto
851 and Waimarino olivine. b) Fo vs. CaO in olivine. CaO concentrations are higher in HAB samples
852 than in Waimarino, Ongaroto, Ohakune and Rotomakariri. Errors are smaller than symbols.

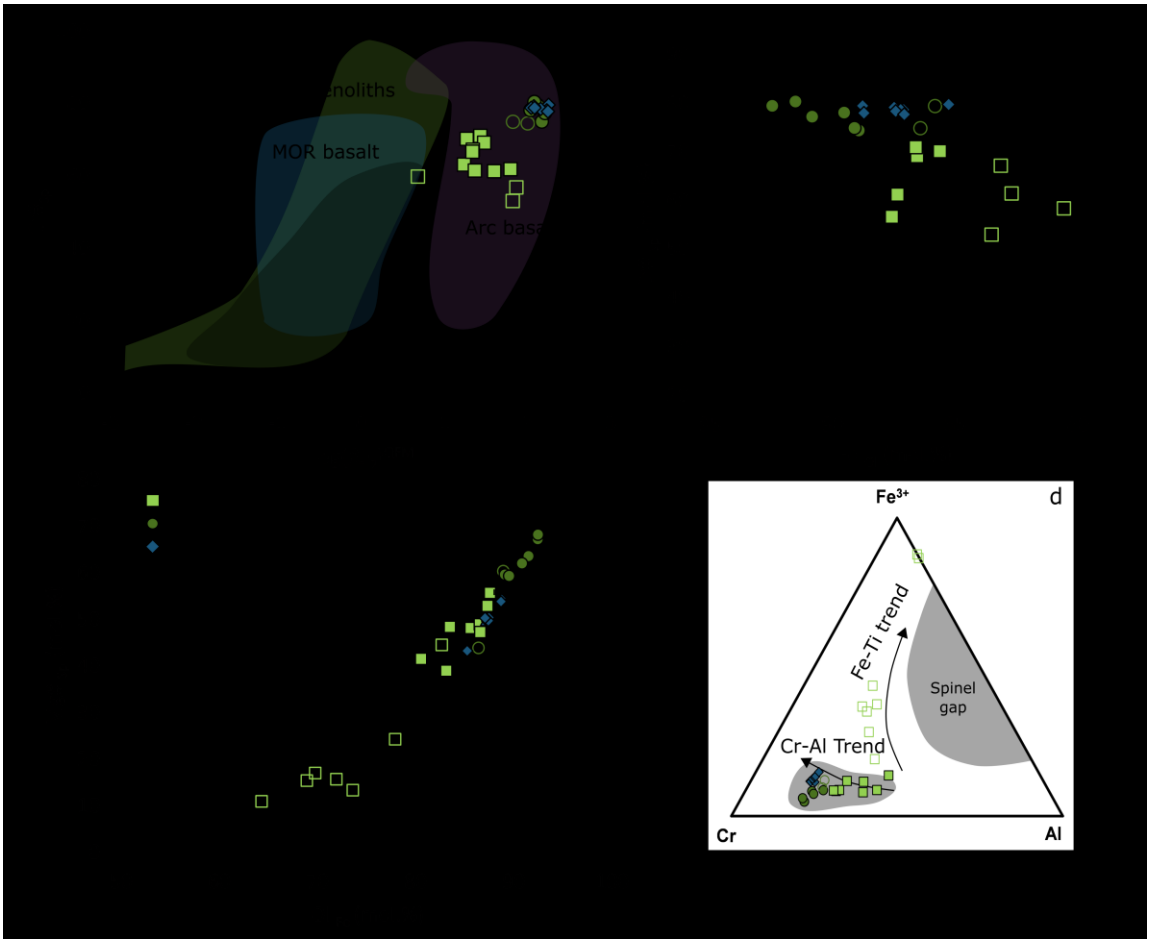

853

854 Figure 4: a) Cr# of spinels vs. log fO_2 (expressed as deviation from the QFM buffer). fO_2 calculated
855 using the method of Ballhaus et al. (1991). Compositional fields also from Ballhaus et al. (1991). b)
856 Cr# of spinel inclusions vs. forsterite content of host olivine. OSMA (Olivine Spinel Mantle Array)
857 and direction of mantle depletion from Arai (1994). c) Mg# of spinel inclusions vs. forsterite content
858 of host olivine. Mantle and magmatic fields also from Arai (1994). d) Proportions of trivalent ions in
859 spinel. Compositional trends from Barnes and Roeder (2001). Filled coloured symbols represent
860 spinel inclusions from cores of olivines. Empty symbols with coloured rims represent spinel
861 inclusions near the rims of olivines.

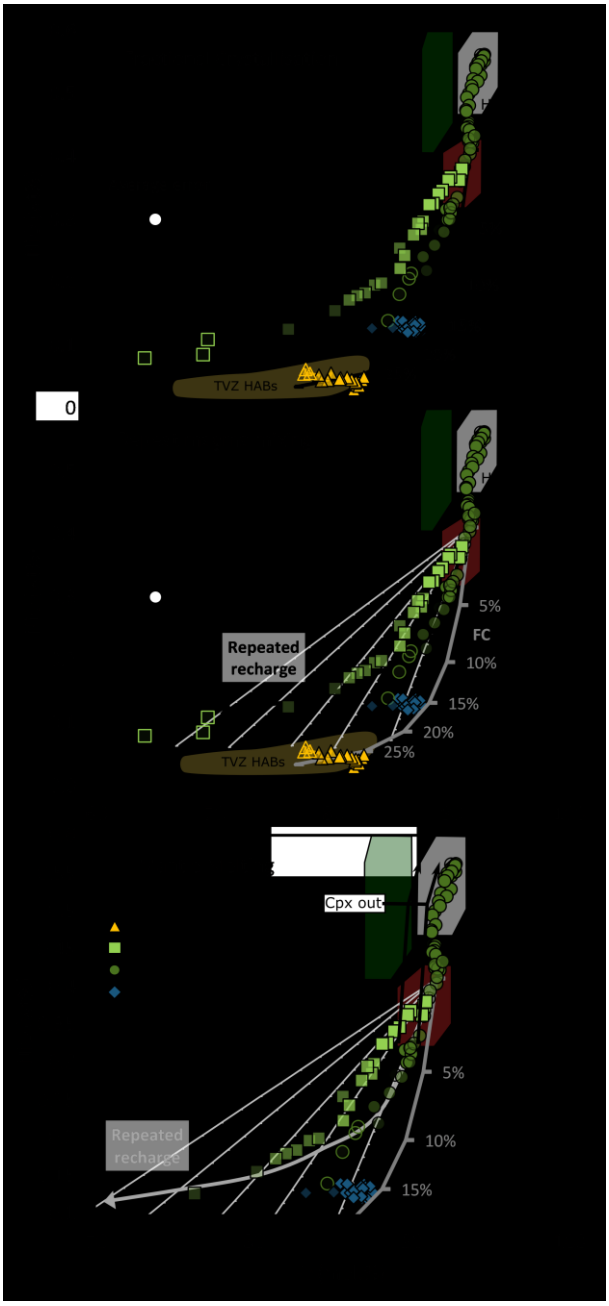

862

863 Figure 5: NiO vs. Fo contents of olivines showing the results of modelling. a) Trajectory of fractional
864 crystallisation model using *Petrolog* (Danyushevsky and Plechov, 2011) and the model of Beattie
865 (1993). b) Trajectory of repeated magma mixing events, adapted from Gleeson and Gibson (2019)
866 and Straub et al. (2011). c) Trajectory of mantle olivine composition at increasing fractions of melt
867 extraction modelled using MELTS (Asimow and Ghiorso, 1998; Ghiorso and Sack, 1995). Mantle
868 compositional fields from Straub et al. (2011) and Workman and Hart (2005). Opaque symbols
869 represent crystal cores, translucency increases towards rims.

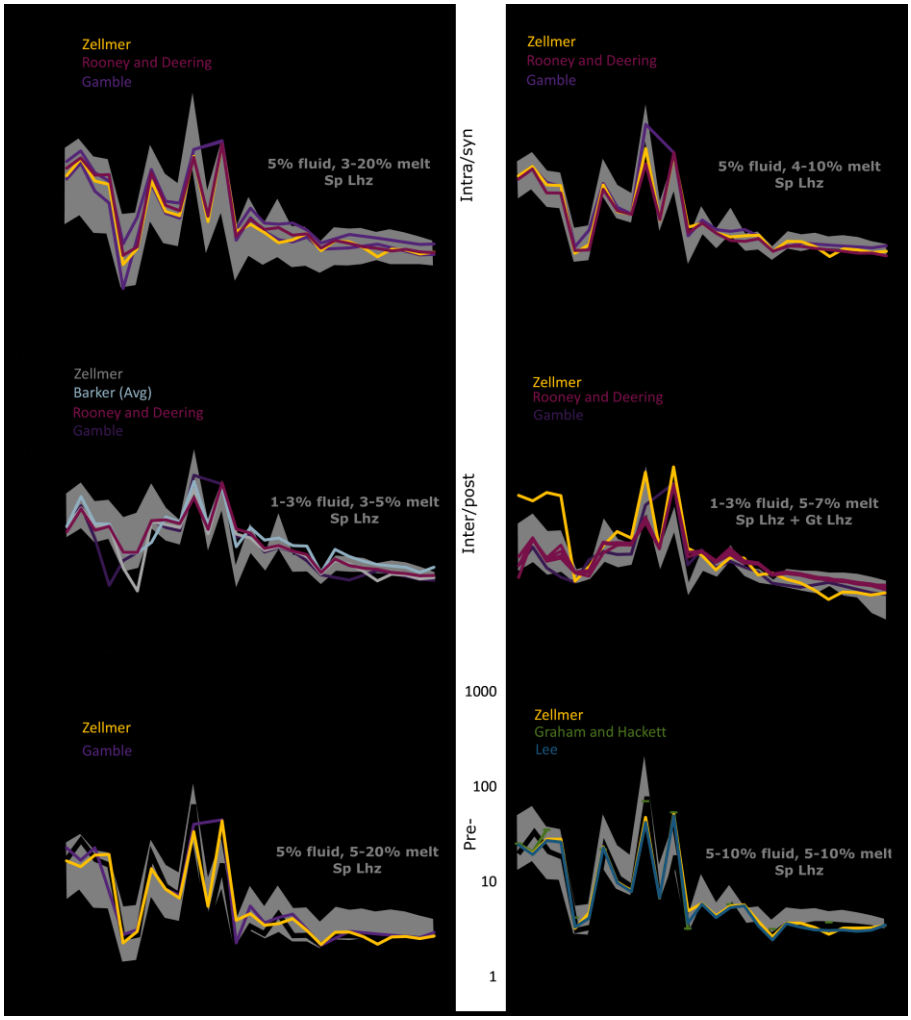

870

871 Figure 6: Primitive-mantle-normalised (Sun and McDonough, 1989) trace element plots of samples
872 from syn-, post- and pre-caldera-forming settings. Zellmer = Zellmer et al. (2020), Barker = Barker
873 et al. (2020), Rooney and Deering = Rooney and Deering (2014), Gamble = Gamble et al. (1993),
874 Lee = Lee (2010). Grey shading shows modelled compositions. Models were created using deep
875 (garnet lherzolite) and shallow (spinel lherzolite) depleted mantle (compositions from Salters and
876 Stracke (2004)), fluid composition from Kogiso et al. (1997) and Gamble et al. (1996), element
877 mobility from Tatsumi and Kogiso (1997), and non-modal batch melting. Best fit ranges are in bold
878 grey text for each sample. Solid black line on Waimarino and Ohakune is modelled mantle melting
879 from a hybrid pyroxenite-peridotite source.

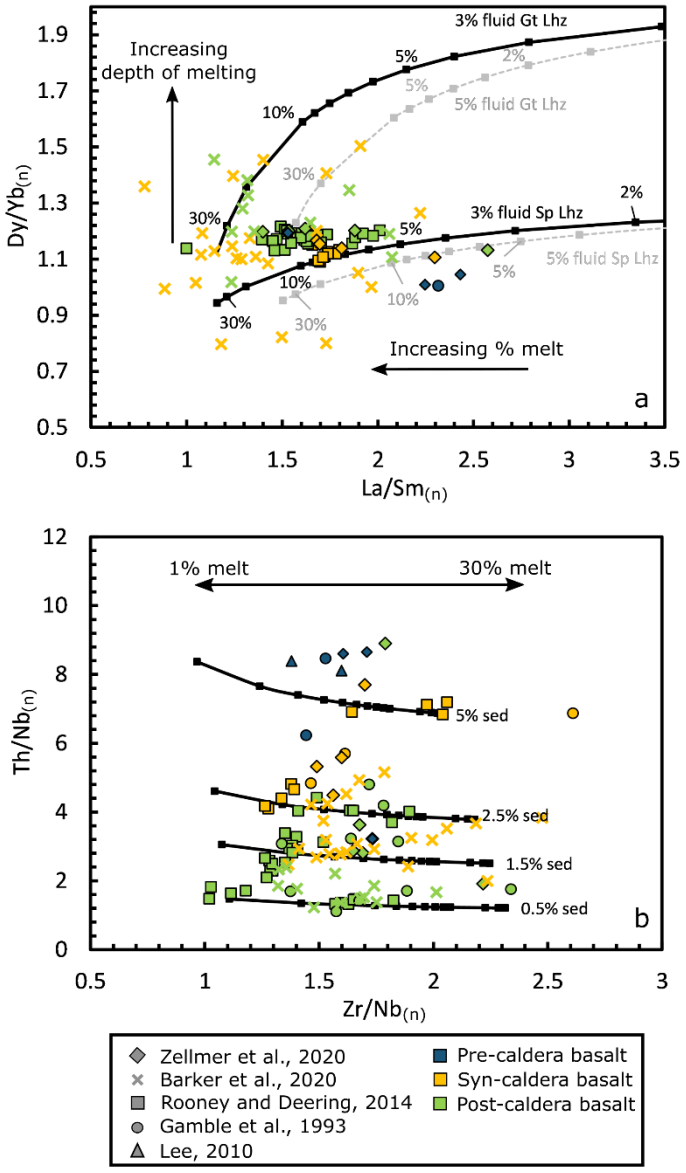

880

881 Figure 7: Primitive-mantle-normalised trace element ratio plots of samples from intra- or syn-
882 caldera, inter- or post-caldera and pre-caldera forming settings. Primitive mantle values from Sun
883 and McDonough (1989). A) Models were created using deep (Gt Lhz) and shallow (Sp Lhz) depleted
884 mantle (compositions from Salters and Stracke (2004)). Grey dashed line shows the effect of
885 additional fluid contribution to the models. Fluid composition from Kogiso et al. (1997) and Gamble
886 et al. (1996), element mobility from Tatsumi and Kogiso (1997), and non-modal batch melting. B)
887 All models produced from spinel lherzolite compositions (Salters and Stracke, 2004); using garnet
888 lherzolite has no effect on the model. Sediment compositions from Gamble et al. (1996).

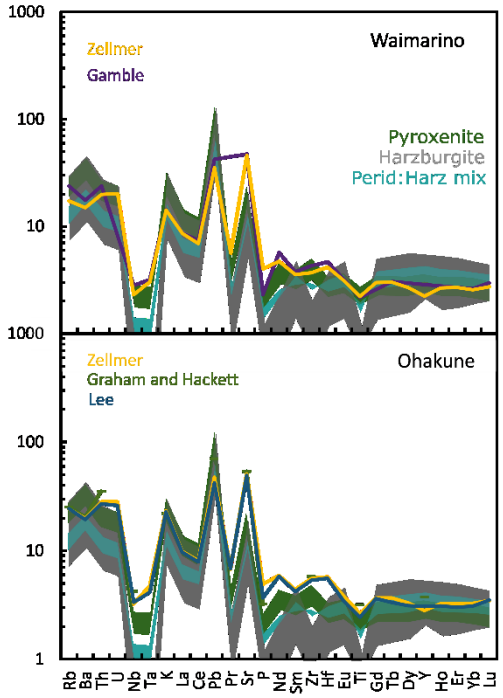

889

890 Figure 8: Primitive-mantle-normalised (Sun and McDonough, 1989) trace element plots of samples
891 from pre-caldera-forming settings. Sources of data are as in Fig. 6. Shaded areas show modelled
892 mantle melts. Pyroxenite melt composition was produce by mixing modelled pyroxenite and
893 peridotite partial melts in ratios of 1:10, respectively. Harzburgite melt composition was produced by
894 partially melting a residue of DM (Salters and Stracke, 2004) after 20% prior melt extraction.
895 Peridotite:Harzburgite mixed composition was produced by mixing a peridotite partial melt with
896 harzburgite partial melt in ratios varying from 10:1, to 50:50. For details of models, see text.
897 Depleted mantle composition, trace element partition coefficient, fluid compositions, and trace
898 element mobilities are as in Fig. 6.

899

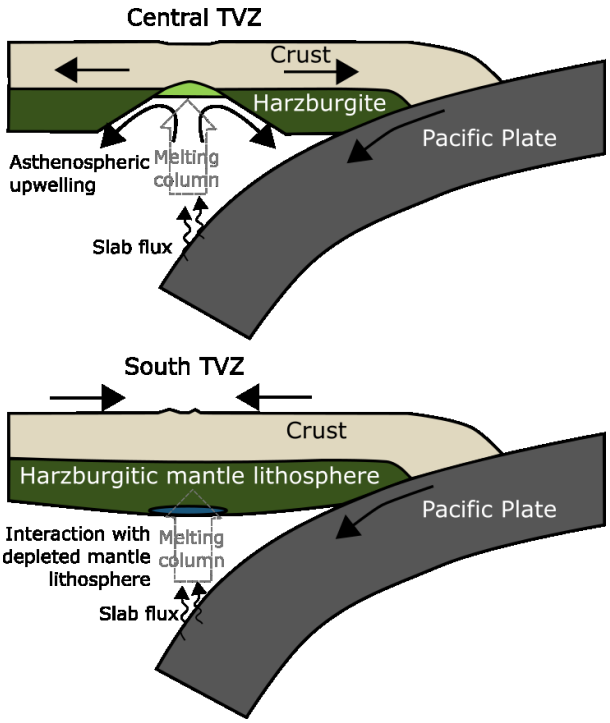

Figure 9: Schematic cartoon illustrating the effect of rifting on the depleted lithospheric mantle, adapted from Stern et al. (2006). South TVZ magmas are generated in the mantle wedge but interact with SCLM on ascent, promoting inheritance of harzburgitic olivine xenocrysts (Waimarino) and deeper stalling of magma (e.g. Ohakune - dark blue). Central TVZ magmas are still generated in the mantle wedge but rifting pulls apart the SCLM leading to inheritance of lherzolitic olivine xenocrysts and promoting shallower stalling and underplating of magma (e.g. Ongaroto - pale green).